

Article

Leveraging Dion–Jacobson Interface Hierarchies for Defect Alleviation in High-Efficiency and Durable Perovskite Solar Cells

Jianxiao Bian ^{1,*} , Yuncong Zhang ², Yang Liu ¹ and Xiaonan Pan ¹¹ School of Intelligent Manufacturing, Longdong University, Qingyang 745000, China² Shaanxi Zhongtian Rocket Technology Co., Ltd., Xi'an 710000, China

* Correspondence: jxbian@ldxy.edu.cn

Abstract: The noteworthy stability of Dion–Jacobson (DJ) phase two-dimensional perovskites marks them as potential contenders for use in optoelectronic applications. Nonetheless, their proliferation is considerably stymied by the constrained charge transport properties inherent to them. This bottleneck is adeptly navigated by deploying 2D-DJ perovskite top layers, seamlessly integrated on 3D perovskite films. We unveil a novel organic cation salt, 4-(Aminomethyl)piperidine (4AMP), as a potent facilitator for treating perovskite photovoltaic films. By employing the annealing technique, we facilitated the in situ creation of a hybrid 2D/3D architecture. Contrasted with conventional 3D architectures, the delineated perovskite heterojunctions with a 2D/3D structure exhibit superior enhanced charge separation, and mitigate photovoltaic losses by proficiently passivating intrinsic defects. The size-graded perovskite 2D/3D structure engineered herein significantly elevates the charge transfer performance, concurrently attenuating the excess lead iodide induced by bulk defects. This precise method resulted in a significant increase in Power Conversion Efficiency, reaching 23.08%, along with an open-circuit voltage (Voc) of 1.17 V. Remarkably, the unpackaged modified device robustly retains 92% of its initial PCE post a 3000 h sojourn under ambient conditions. This discourse propounds a novel paradigm for constructing stable planar PSC 2D/3D heterojunctions, thereby enriching the blueprint for advanced perovskite-based photovoltaic systems.



Citation: Bian, J.; Zhang, Y.; Liu, Y.; Pan, X. Leveraging Dion–Jacobson Interface Hierarchies for Defect Alleviation in High-Efficiency and Durable Perovskite Solar Cells. *Processes* **2024**, *12*, 233. <https://doi.org/10.3390/pr12010233>

Academic Editor: Ioannis Spanopoulos

Received: 18 December 2023

Revised: 10 January 2024

Accepted: 18 January 2024

Published: 21 January 2024



Copyright: © 2024 by the authors. Licensee MDPI, Basel, Switzerland. This article is an open access article distributed under the terms and conditions of the Creative Commons Attribution (CC BY) license (<https://creativecommons.org/licenses/by/4.0/>).

Keywords: two-dimensional perovskites; Dion–Jacobson phase; 2D/3D structure; perovskite solar cells; 4-(Aminomethyl)piperidine

1. Introduction

Perovskite Solar Cells (PSCs) have breached certified Power Conversion Efficiencies (PCEs) beyond 26%, courtesy of their superior photoelectric attributes [1–9]. Yet their susceptibility to unstable performance, notably in humid and light-soaking scenarios, poses a predicament for their pragmatic deployment [10–15]. The PCE pinnacle reached hitherto lingers distant from the Shockley–Queisser efficiency frontier, owed to non-radiative charge carrier recombination at bulk and interfacial defects near the contacts of interfacing perovskites with charge transport layers [16]. This underscores the imperative of perovskite film interface engineering to foster high-efficiency, robust planar PSCs [17–21]. Low-dimensional perovskites have emerged as a viable recourse to this quandary, albeit their commendable moisture resistance, the protracted hydrophobic alkyl groups of large ammonium salts precipitate a decline in charge transport and PCE [22–24]. Moreover, solution-treated perovskites, being polycrystalline ionic crystals, bear ionic defects like I^- and Pb^{2+} vacancies that potentially degrade device performance [25–27]. In addition, solution-treated perovskite is usually a polycrystalline ionic crystal with ionic defects, like I^- vacancies and Pb^{2+} vacancies, which can lead to charge traps and result in degraded device performance [28–30]. Nevertheless, macro-organic ammonium ions can obviate these ionic defects by coordination with Pb^{2+} [31].

Lately, the development of 3D/2D heterojunction perovskite devices has been achieved, integrating the superior photovoltaic efficiency of 3D perovskite with the remarkable environmental stability of 2D perovskite [32–34]. Furthermore, the 2D/3D perovskite heterojunction not only improves the stability of the perovskite film but also modulates the energy band levels in high-performance Perovskite Solar Cells (PSCs) [35]. Considered to be one of the most crucial surface modifiers, large organic ammonia salts, such as octyl ammonium iodides, can be directly used to passivate the surface by combining with lone pair electrons to control the defects and eliminate charge traps [36]. Nonetheless, the extended chain organic linkers hinder charge transport from 3D to 2D perovskite, as the bulky organic molecules exist in an electrically insulated state [37].

To optimize the charge delivery property of the 2D capping layer and to further minimize the defect states, we concentrated on the composition improvement at the 2D–3D intersection using a Dion–Jacobson (DJ) perovskite capping layer. DJ perovskites have a $A'A_{n-1}B_nX_{3n+1}$ general formula with A' being a diammonium organic compound [38–40].

In our endeavor to optimize the charge delivery characteristic of the 2D capping layer and attenuate defect states, we focused on composition refinement at the 2D–3D nexus utilizing a Dion–Jacobson (DJ) perovskite capping layer. Unlike RP phase perovskites with single ammonium cations, DJ phase perovskites harbor double ammonium cations, conferring structural and device stability. In this study, we introduce the innovative use of a hydrazone compound, 4-(Aminomethyl)piperidine (4AMP), as an interfacial ionic solution. This approach is employed to create a 2D perovskite layer on a 3D CsFAMA perovskite, subsequently engineering the interface with the hole transporting layer [36–38]. Through meticulous post-treatment annealing temperature and solution concentration optimization, diverse 2D capping layers are achieved. The merits of 4AMP selection encompass enhanced charge transport, device stabilization, and defect mitigation attributed to its flexible alkyl chain configuration. This approach combines the hydrophobic nature and defect minimization characteristics of 2D DJ perovskite with the high photovoltaic efficiency of 3D perovskite. This leads to the development of optimized 2D/3D Perovskite Solar Cells (PSCs) that not only achieve a Power Conversion Efficiency (PCE) of 23.08% but also maintain stability for over 3000 h.

2. Results

2.1. Morphology

We harnessed the mixed perovskite CsFAMA as the photonic absorptive material, and the corresponding perovskite films were synthesized employing a quintessential one-step spin-coating technique as formerly elucidated. The exhaustive fabrication blueprint of the 2D/3D perovskite films through a bifurcated surface passivation modality is expounded in the experimental segment. Subsequent to the genesis of the active stratum, 4AMP dissolved in IPA solution was bestowed onto the perovskite layer and spin-coated to engender a low-dimensional veneer layer.

To probe further into the interface engineering ramifications, we initially scrutinized the surface topography and crystalline integrity of the optimized 2D/3D films via top-view SEM imaging (Figure S1). A smattering of PbI_2 crystals, with dimensions approximating ~200 nm, were discernible on the facade of the control perovskite films, attributable to the surfeit PbI_2 in the precursor amalgam and the deficient reactive process for organic ions volatilization amidst the annealing process (Figure S1, Supporting Information). The introduction of 4AMP transformed the surface morphology of the CsFAMA perovskite film, owing to the formation of a 2D perovskite layer on the surface. Figure S1 illustrates that the 4AMP regimen metamorphosed the coarse surface and diminutive crystal grains into a planar, uniform, and dense topography. Moreover, 4AMP efficaciously recrystallized the perovskite and augmented the grains. The diminutive long-chain molecules proficiently passivated the iodine voids at the interface and grain boundaries, catalyzing a secondary growth continuum.

Especially for the 4AMP-amended perovskite film, we attained a uniform, compact, and planar film with a grain dimension transcending 400 nm, which is imputed to the promotion of the in situ secondary growth of perovskite grains by the long-chain molecules 4AMP. The refined 2D capping layer not only improved surface irregularities and reduced interfacial charge loss but also initiated the secondary crystal growth of perovskite, a crucial aspect in the fabrication of high-quality devices. Additionally, we compared the root mean square (RMS) value extracted from the correlative height sensor AFM imagery of the perovskite film (Figure 1C,D). The outcomes, gauged at 69.86 nm and 42.59 nm for the control and 4AMP-amended perovskite film, respectively, underscore the vantage in concocting high-quality films.

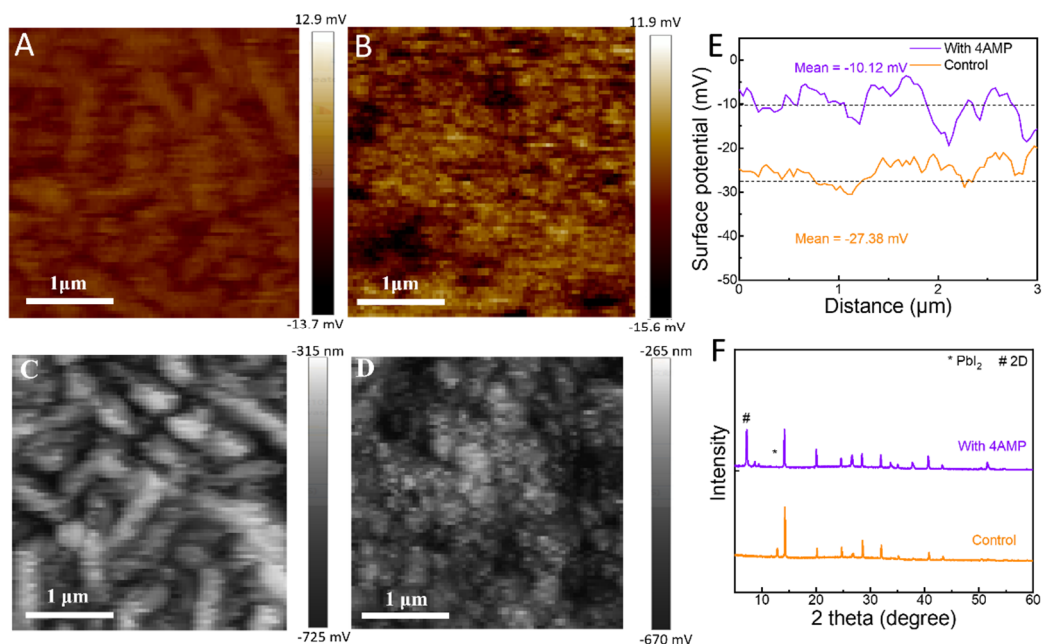


Figure 1. This figure presents the KPFM images of perovskite films, with (A) showing the control and (B) depicting the 4AMP-modified variant. Part (E) illustrates the Contact Potential Difference (CPD) measured along the solid black lines indicated in (A,B). Additionally, AFM height sensor images are provided for the control (C) and 4AMP-treated (D) perovskite films. Finally, (F) displays the XRD patterns of the perovskite films, comparing the control with the 4AMP-modified samples.

The UV–vis absorption data and absorption coefficients data presented in Figure S2 indicate that the 4AMP-modified perovskite film exhibited the most significant enhancement in light absorption among the perovskite films, aligning well with the findings from the SEM analysis. The interface characteristics and the rationale for bolstered electrical performance metrics with 4AMP modulation were further dissected employing Kelvin Probe Force Microscopy (KPFM). The CPD mappings featured in Figure 1A,B were used to scrutinize the work function, aid in assessing the open-circuit voltage (V_{oc}) enhancement, and to examine the potential for structural distortions such as ribbon buckling near grain boundaries. Given the superior work function of the metallic tip vis-a-vis that of the perovskite surface, an enlarged CPD typically correlates with a pronounced work function disparity between the tip and the specimen (Figure 1E). The significant shift in surface potential suggests a transition in the Fermi energy level, favorable for enhanced energy band alignment in the device. The comparatively higher CPD indicates a raised Fermi energy level, contributing to an increased built-in potential. This observation is consistent with the improved open-circuit voltage (V_{oc}) in 4AMP-modified PSCs, likely attributed to the Fermi energy level nearing the conduction band. This implies a more n-type surface, beneficial for facilitating excess hole transport. In this vein, it can be inferred that 4AMP modulation to enhance the photovoltaic attributes of perovskite apparatuses may relate to

these two interfaces. To intricately examine the compositions, we executed XRD patterns for control and modulated perovskite films with 4AMP modulation in Figure 1F. The amplification of the characteristic peaks of 2D perovskite was noted when utilizing the 4AMP-modulated perovskite film, and the 2D perovskite was triumphantly grown in situ on the 3D perovskite. We also scrutinized the impact of divergent annealing temperatures on the surface crystallization of the perovskite.

2.2. Photovoltaic Performance of the PSC

Figure 2A presents the chemical structure of 4-(Aminomethyl)piperidine (4AMP), utilized for enhancing the surface of the perovskite materials in our study. As illustrated, 4AMP embodies two alkyl groups and a rigid benzenoid ring. The alkyl chains, characterized by their flexibility and hydrophobic nature, facilitate seamless integration into the perovskite lattice, leading to the formation of 2D perovskite phases on the surface of the 3D perovskite. Figure 2B unveils a cross-sectional scanning electron microscopy (SEM) depiction of a complete PSC, with optimal thicknesses demarcated as 50, 600, 250, and 100 nm for SnO₂, 3D/2D perovskite, Spiro-OMeTAD, and gold layers, respectively. The perovskite film, created using a conventional one-step spin-coating method, exhibited a remarkable transformation from 3D to 2D perovskite on the surface, as depicted in Figure 2B. This change can be further manipulated through the annealing process. An investigation into the influence of 4AMP modification concentration on device attributes was undertaken.

The current density–voltage (J–V) profiles of the PSCs are exhibited in Figure 2C, with pertinent photovoltaic parameters consolidated in Table 1. Figure S3 provides detailed statistics for the Power Conversion Efficiency (PCE), open-circuit voltage (V_{OC}), fill factor (FF), and current density (J_{SC}) across 10 individual cells. It highlights the enhanced reproducibility and PCE in 3 mg/mL 4AMP-modified Perovskite Solar Cells (PSCs). Notably, these modified cells achieved a record PCE of 23.08% and an average of 22.36%. Specifically, the unmodified (control) devices reached a peak PCE of 19.21% with a J_{SC} of 24.06 mA·cm⁻², a V_{OC} of 1.07 V, and a FF of 74.61% in reverse scan (RS), and a PCE of 20.33% (with a J_{SC} of 24.08 mA·cm⁻², a V_{OC} of 1.07 V, and a FF of 78.90%) in forward scan (FS). In contrast, the top-performing 4AMP-modified device showed a PCE of 23.08% (with a J_{SC} of 24.25 mA·cm⁻², a V_{OC} of 1.17 V, and a FF of 81.34%) in RS, and a PCE of 22.36% (with the same J_{SC} and V_{OC} , but a FF of 79.11%) in FS. The addition of 4AMP significantly reduced hysteresis, likely due to effective passivation of the surface and crystalline boundary defects as well as the inhibition of ion migration.

Table 1. An outline of the photovoltaic characteristics of the highest-performing devices, comparing those prepared without and with 4AMP treatment.

Samples	Scanning Direction	V_{OC} (V)	J_{SC} (mA·cm ⁻²)	FF (%)	PCE (%)
Control	RS	1.06	24.13	79.48	20.33
	FS	1.06	24.07	75.25	19.20
With 4AMP	RS	1.17	24.24	81.37	23.08
	FS	1.17	24.17	79.06	22.36

Figure 2D illustrates the stabilized maximum current density (J_{max}) for both the control and 4AMP-enhanced Perovskite Solar Cells (PSCs), as determined at the Maximum Power Point (MPP). For the control and 4AMP-enhanced devices, the maximum voltage (V_{max}) achieved was 1.06 V and 0.96 V, respectively, while the maximum current (I_{max}) reached 2.3 mA and 2.2 mA. When subjected to continuous illumination in ambient air for 180 s, both the modified and control devices maintained a steady-state current density (J_{SC}) of 22.86 mA·cm⁻² and 21.94 mA·cm⁻², respectively. The J–V characteristics of the electron transmission devices, configured as FTO/SnO₂/3D perovskite/4AMP-2D

perovskite/PCBM/Au, were compiled to evaluate the electron trap-state densities. This evaluation was based on the trap-filled limit voltage (V_{TFL}), using a specific equation:

$$V_{TFL} = \frac{L^2 en_t}{2\epsilon\epsilon_0}, \quad (1)$$

The equation for calculating the trap-state density (n_t) involves the electron charge (e), the thickness of the 3D perovskite/4AMP-2D perovskite layer (L), the relative dielectric constant (ϵ_0), and the vacuum permittivity (ϵ , approximately 35). Using this formula, the trap-filled limit voltage (V_{TFL}) values for both the modified and control devices were determined to be 0.35 V and 0.70 V, respectively. These V_{TFL} measurements indicate a lower trap density in the modified device, with n_t values of $5.39 \times 10^{15} \text{ cm}^{-3}$ for the modified device and $10.8 \times 10^{15} \text{ cm}^{-3}$ for the control device, as shown in Figure 2E.

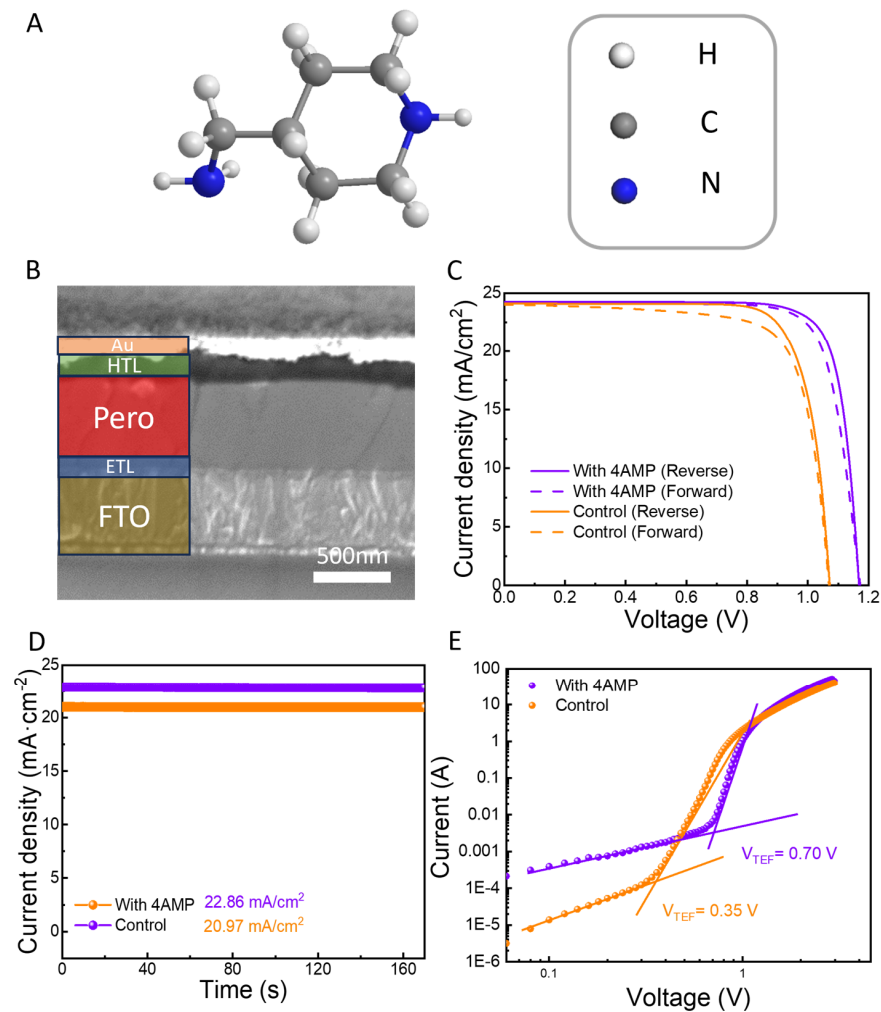


Figure 2. (A) displays the chemical structure of 4-(Aminomethyl)piperidine (4AMP). (B) presents a cross-sectional Scanning Electron Microscope (SEM) image, which vividly exhibits the detailed structure of the 4AMP-modified PSCs. (C) The current–voltage (J–V) curves of the devices, both with and without the 4AMP modification, are shown. These curves were measured in both reverse scan (RS) and forward scan (FS) modes at a scan rate of 100 mV/s. (D) tracks the current density over a duration of 180 s. Finally, (E) provides the dark J–V curves for electron-only devices, comparing the characteristics of devices with and without 4AMP modification. Additionally, the figure’s inset illustrates the specific structure of these electron-only devices, which includes layers of Fluorine-doped Tin Oxide (FTO), tin dioxide (SnO_2), perovskite, [6,6]-Phenyl-C61-butyric acid methyl ester (PCBM), and gold (Au).

The elucidation of internal electron dynamics is astutely depicted via impedance spectroscopy (IS) spectra under dark conditions (Figure 3A). The device, post-modification, manifested a heightened recombination resistance (R_{reb}) value of 147Ω , a stark contrast to the 21Ω found in the control device, a testament to the effectively curtailed recombination rate as discerned from the impedance standpoint. Additionally, the delineation of V_{OC} as a function of the light intensity furnished nuanced insights into the recombination processes triggered by diverse trap states within the devices (Figure 3B). Such relations can be meticulously expressed by the following equation:

$$\delta V_{\text{OC}} = n \left(\frac{K_B T}{e} \right) \ln(I) + \text{constant} \quad (2)$$

where $n = 1.25$ signifies the ideality factor, K_B the Boltzmann constant, e the elementary charge, T the absolute temperature, and I the light intensity. Significantly, the slope of the J-V curves for the 4AMP-modified Perovskite Solar Cells (PSCs), characterized by a lower ideality factor ($n = 1.32$), was more gradual compared to that of the control device (with $n = 1.41$). This observation is indicative of effectively reduced trap-induced carrier recombination in the modified PSCs. Furthermore, the scatter found in the data points for the device with 4AMP is notable. Since this is a single dataset, the precision in representing error using standard deviation or standard error is limited. Therefore, we have opted for a different approach. The average values for the device with 4AMP are 1.1083 and 1.007. The aforesaid electrical properties characterization unequivocally underscores the reduction in the trap states for carrier recombination subsequent to the 4AMP introduction, a favorable condition for enhancing the charge extraction efficiency.

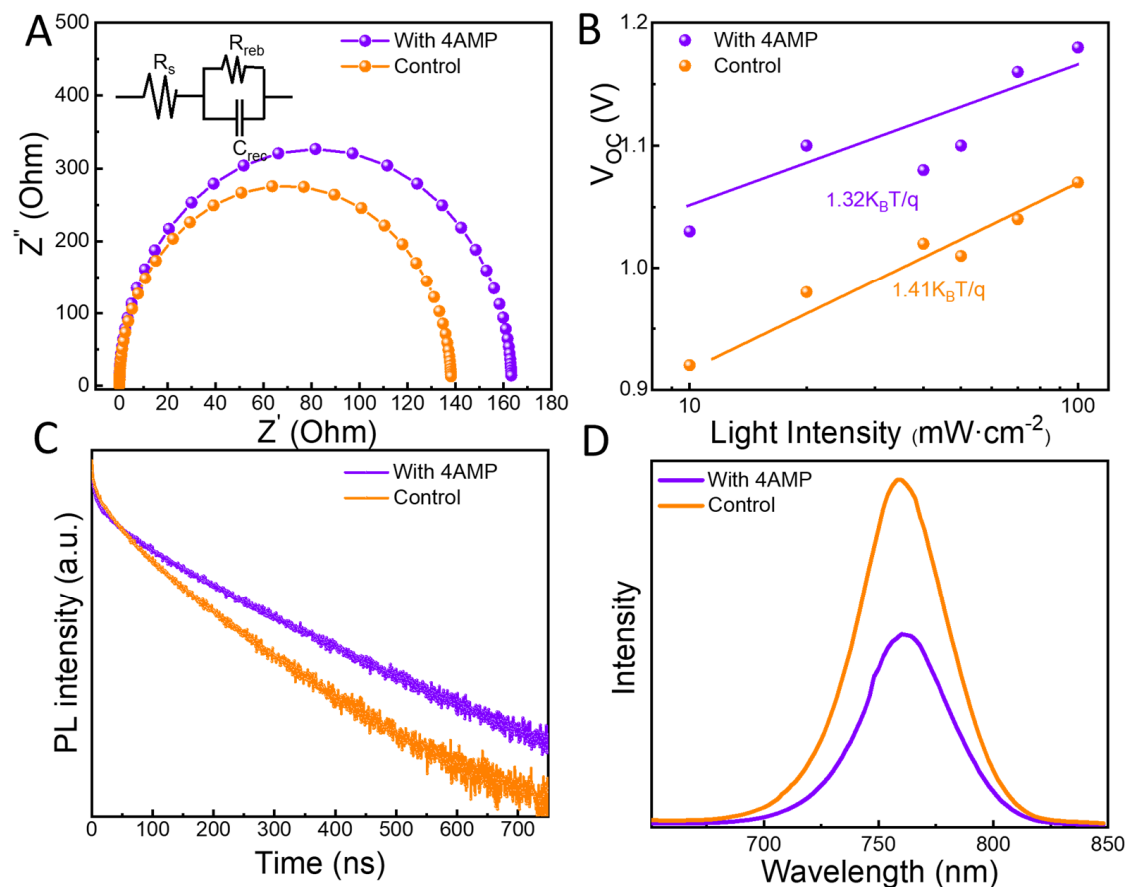


Figure 3. (A) features Nyquist plots, measured at 0 V across a specific frequency range from 1 Hz to 0.1 MHz in dark conditions, for the optimal and control devices. These plots are crucial for assessing

the impedance characteristics of the solar cells. (B) The light-intensity-dependent open-circuit voltage (V_{OC}) for both the control and the 4AMP-modified PSCs is illustrated, offering insights into how V_{OC} varies with changing light intensities. (C) showcases the Time-Resolved Photoluminescence (TRPL) curves for the perovskite films, which are instrumental in determining the lifetime of photogenerated carriers, a vital aspect for solar cell efficiency. (D) displays the photoluminescence (PL) spectra of perovskite films deposited on glass substrates, providing a detailed look into the optical properties of these films, including crucial factors like bandgap and exciton recombination.

In Figure 3D, the 4AMP-modified films demonstrate a notably lower photoluminescence (PL) peak intensity compared to the control films. This suggests that 4AMP effectively suppresses exciton recombination in the device. Additionally, the PL peak of the 4AMP-modified film shows a redshift, aligning with the found bandgap narrowing in these films. Moreover, the corresponding time-resolved PL curves, as shown in Figure 3D, indicate that the modified device exhibits a shorter lifetime, evidenced by the faster decay trace with a time constant (τ_1) of 5.12 ns. The detailed PL decay constants, calculated using a bi-exponential equation, are compiled in Table S1 in the Supporting Information section. It was found that the decay lifetime for the perovskite film modified with 4AMP is longer (6.68 ns) compared to that of the control film. These results collectively imply that the incorporation of 4AMP not only affects the optical properties of the perovskite films but also significantly enhances their electron extraction capability.

To meticulously appraise the long-term stability of the layers, we orchestrated a systematic documentation of photographs pertaining to the unencapsulated perovskite films under the stringent conditions of high relative humidity (RH) stress testing at $80 \pm 10\%$ (Figure 4A). A discernible resilience was exhibited by the 4AMP-modified films, which astonishingly presented no visible alteration post a 15-day storage duration, a stark contrast to the control perovskite films. Concurrently, an examination of the UV-Vis absorption intensity, as depicted in Figure 4B, unraveled a precipitous decline over time for the control films, whilst the 4AMP-modified counterparts manifested only a marginal decrement. Further corroborating these observations, the XRD pattern, as illustrated, resonates well with the UV-vis spectral data. Post a 15-day ageing period, a pronounced PbI₂ peak emanates from the control film, indicative of perovskite decomposition. Conversely, the 4AMP-modified film, even post the identical ageing timeline, staunchly retains a robust perovskite peak, thereby affirming the preservation of the perovskite structural integrity. Furthermore, a compelling variance in water contact angles was found; a relatively modest angle of 51.9° was exhibited by the control 3D perovskite film, whereas a markedly elevated angle of 76.2° was displayed by the 4AMP-modified film (Figure 4C). The marked rise in the water contact angle is a strong indicator of the impervious characteristics of the low-dimensional capping layer. This layer acts efficiently to block water from entering the perovskite lattice, thereby substantially increasing the material's resistance to moisture. For the stable analysis, the 4AMP-modified device exhibited an enduring resilience, displaying no discernible decomposition even after a protracted 3000 h exposure at 40% relative humidity, whilst retaining an impressive 88% of its initial PCE. On the flip side, the control PSCs witnessed a precipitous PCE plunge to a mere 40% of its nascent value (Figure 4D). The cumulative evidence of superior quality and enduring stability unequivocally propels our avant-garde devices to a vantage point of significant promise for practical implementations. The robustness of the 4AMP-modified films under a gamut of adverse environmental conditions underscores the profound potential of 4AMP as a quintessential modifier for advancing the frontier of perovskite solar cell technology.

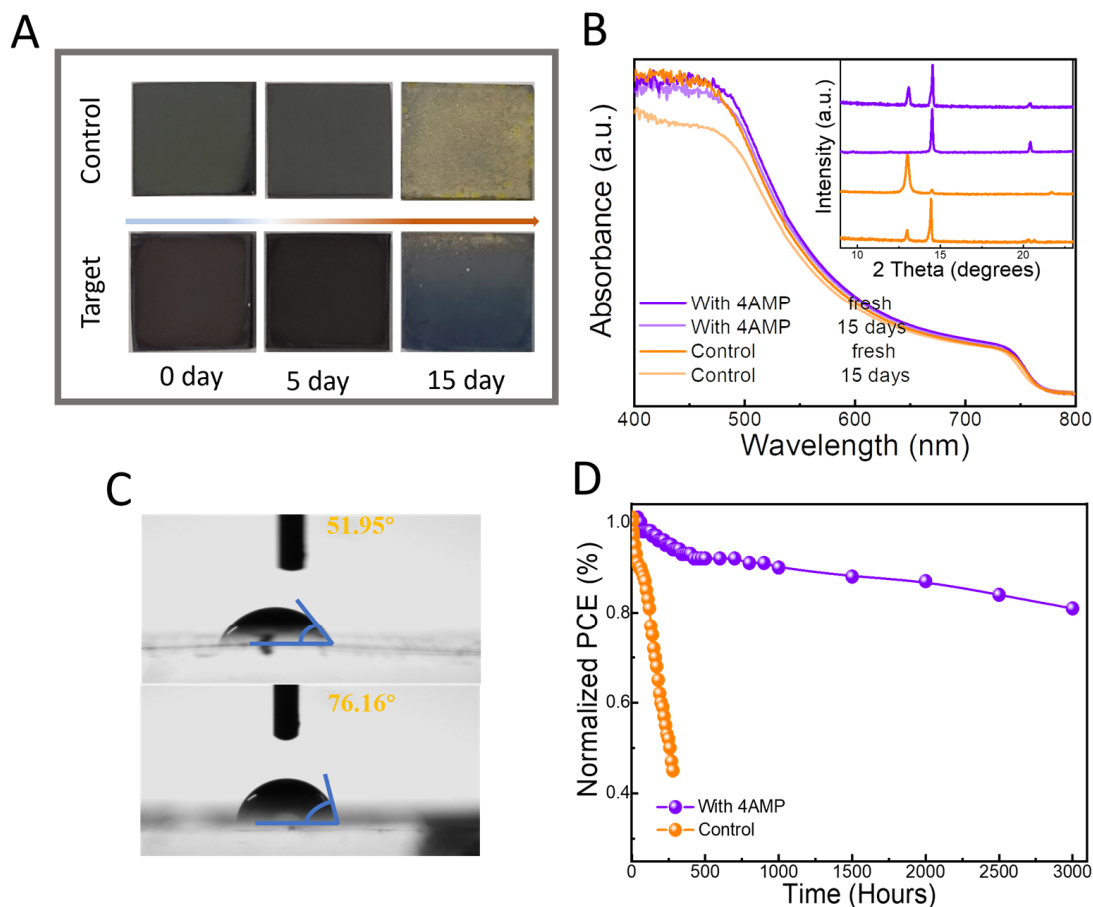


Figure 4. (A) features photographs of these films after being subjected to high humidity conditions ($80 \pm 10\%$ RH) for 15 days, visually demonstrating their response to moisture. (B) presents the UV–visible spectrum and X-ray diffraction (XRD) patterns (seen in the inset) of the films post a 15-day exposure to similar humidity levels, providing insights into their chemical and structural changes. The water contact angles of different perovskite films are measured and displayed in part (C), highlighting the films’ surface hydrophobicity. (D) illustrates the normalized Power Conversion Efficiency (PCE) stability curves for both control and modified encapsulated devices in a 40% relative humidity environment, comparing their long-term performance under these specific conditions.

3. Conclusions

In our research, we incorporated 4-(Aminomethyl)piperidine (4AMP), a large organic di-ammonium salt, to create a 2D/3D heterojunction. This was achieved by optimizing the composition to include a high n -value of the Dion–Jacobson (DJ) 2D phases, while minimizing the residual 4AMP molecules. Our method involved a straightforward process of spin-coating followed by thermal treatment. By carefully adjusting the post-annealing temperature, we successfully formed a 4AMP-based low-dimensional perovskite layer on top of the CsFAMA perovskite. This addition notably contributed to effective interface or grain boundary passivation. The introduction of this organic molecule significantly improved the crystallinity of the material and eradicated interfacial defects, thus substantially reducing nonradiative recombination. As a result, we found a remarkable enhancement in the Power Conversion Efficiency (PCE), increasing from 20.33% to 23.08%. This improvement was attributed to the effectively passivated surface defects and the reduced charge carrier recombination. Moreover, the DJ 2D perovskite capping layer that we developed proved to be highly effective in preventing moisture intrusion into the perovskite lattice, thereby improving the moisture stability of the material for more than 60 days under high relative humidity conditions. Our novel approach to fabricating hierarchical interface perovskite presents a promising pathway for developing highly efficient and stable Perovskite Solar

Cells (PSCs) in ambient air conditions. By crafting a stabilizing 2D perovskite capping layer over 3D perovskites, this technique paves the way for the commercial realization of perovskite-based photovoltaic technology.

4. Experiment Section

4.1. Materials

Cesium iodide (CsI), Lead iodide (PbI₂), and Lead bromide (PbBr₂) was purchased from Xi'an Polymer Light Technology Corp. (Xi'an, China). FAI, MAI, MABr, 4-(Aminomethyl) piperidine was purchased from Greatcell Solar Limited. Dimethylsulfoxide (DMSO), N,N-Dimethylformaldehyde (DMF), and isopropanol (IPA) were purchased from Macklin Inc (Shanghai, China). SnO₂ was obtained from Sigma-Aldrich (St. Louis, MO, USA). FTO glass, [6,6]-phenyl-C61-butyric acid methyl ester (PCBM) and Spiro-OMeTAD were purchased from Liaoning YouXuan Technology Co., Ltd. (Dalian, China). All chemicals contained herein were used without further purification.

4.2. Device Fabrication

The Fluorine-doped tin oxide (FTO) glass substrates were ultrasonically cleaned in a FTO cleaning solution, deionized water, and ethanol for 20 min, respectively. Then, they were treated in an ultraviolet UV/ozone cleaner for 10 min to improve the surface wettability of FTO glass. Next, the SnO₂ electron transport layer was prepared by spin-coating SnO₂ precursor solution (2.67%, in water) onto FTO substrates at 3000 rpm for 30 s and annealed on a hotplate at 150 °C for 30 min. The CsFAMA precursor solution was prepared by dissolving 0.172 g of Formamidinium iodide (FAI), 0.0224 g of methylammonium bromide (MABr), 0.507 g of PbI₂, and 0.0734 g of PbBr in 1 mL mixed solution of DMF and DMSO (volume ratio 4:1). Then, 0.320 g of CsI was dissolved to 1 mL DMSO. A total of 50 µL of this solution was added to the previous perovskite solution. The prepared Cs_{0.05}(FA_{0.83}MA_{0.17})_{0.95}PbI_{0.83}Br_{0.17} perovskite precursor solution was spin-coated onto the FTO/SnO₂ substrate at 600 rpm for 5 s and 4000 rpm for 30 s, respectively, then the original 3D perovskite film was directly annealed at 110 °C for 60 min. After that, the samples were treated by N-DENCl₂ under the N₂-filled glovebox. 4AMP was dissolved in IPA and spin-coated onto the perovskite surface at 3000 rpm. for 15 s prior to being annealed at 110 °C on a hotplate. Subsequently, the Spiro-OMeTAD solution prepared by mixing 100 mg of Spiro-MeOTAD, 45 µL of 4-tert-butylpyridine, and 45 µL of acetonitrile solution containing 340 mg mL⁻¹ of lithiumbis-(trifluoromethylsulfonyl) imide in 2 mL of chlorobenzene was deposited on the surface of 2D/3D and 3D perovskite layer and spin-coated at 3000 rpm for 30 s in an atmosphere full of nitrogen. Finally, a 100 nm thick Au electrode was deposited by thermal evaporation in a vacuum environment (4×10^{-4} Pa) to form a FTO/SnO₂/Perovskite/Spiro-MeOTAD/Au final device. The electron transporting devices with a structure of FTO/SnO₂/Perovskite/PCBM/Au were employed to estimate the electron trap-state densities. A total of 10 mg of [6,6]-phenyl-C61-butyric acid methyl ester (PCBM) was dissolved in 1 mL of chlorobenzene. A total of 50 µL of PCBM precursor solution was spin-coated onto the perovskite layer at 1000 rpm for 30 s and sintered at 100 °C for 30 min. The preparation method of the other layers was the same as mentioned above.

4.3. Device Characterizations

The surface morphology of the 3D and 2D/3D perovskite films and the cross-sectional view of the PSCs were found by a JEOL 7610F emission scanning electron microscope (SEM). X-ray diffraction (XRD) patterns for perovskite films were recorded on a Rigaku SmartLab(9Kw)D X-ray diffractometer, using a ray monochromatized Cu K_α target radiation source at a scanning rate of 8°/min. Electrochemical impedance spectroscopy (EIS) was executed by a CHI660 electrochemical station. The absorption spectra were recorded by using a UV-1900 spectrometer (Shimadzu, Kyoto, Japan). The photoluminescence (PL) characterization was carried out by using a fluorescence luminescence spectrometer. The

J-V characteristics were measured under AM 1.5 G irradiation using a 71S type solar simulator system customized from SOFN Instruments Co., Ltd. (Beijing, China), and Keithley 2400 (Cleveland, OH, USA) was employed as a digital sourcemeter. The light intensity was calibrated with a reference silicon cell by comparing standard photocurrent density. By using an Edinburgh Instruments spectrometer (FLS980, Livingston EH54 7DQ, UK), we achieved time-resolved PL (TRPL) spectra and steady-state PL spectra under 480 nm excitation wavelength. The control and 4AMP perovskite film were analyzed by an AFM and KPFM (Keysight 5500 (Santa Rosa, CA, USA) scanning probe microscope, tapping mode, CS-AFMin contact mode) applies a bias voltage of 1 V.

Supplementary Materials: The following supporting information can be downloaded at <https://www.mdpi.com/article/10.3390/pr12010233/s1>, Figure S1: Top SEM images of the perovskite film treated with and without 4AMP; Figure S2: UV absorbance spectra of the perovskite film treated with and without 4AMP; Figure S3: Statistical analysis for 10 individual cells of the effect of different concentration on the FF, J_{SC} , V_{OC} , and PCE; Table S1: The summary of TRPL curve analysis: short and long lifetime contributions and electron lifetimes.

Author Contributions: Conceptualization, J.B.; Methodology, J.B.; Validation, X.P.; Investigation, Y.Z.; Resources, Y.Z.; Writing—original draft, Y.L.; Project administration, J.B. All authors have read and agreed to the published version of the manuscript.

Funding: This work was supported by the Innovation Fund Project of College Teachers of Gansu Provincial Department of Education (2023B-206) and the Crossing Research Project of Longdong University (HXZK2329) and the Gansu Province Higher Education Youth Doctoral Fund Project (2022QB-167).

Data Availability Statement: Data are contained within the article and Supplementary Materials.

Conflicts of Interest: Author Yuncong Zhang was employed by Shaanxi Zhongtian Rocket Technology Co., Ltd. The remaining authors declare that the research was conducted in the absence of any commercial or financial relationships that could be construed as a potential conflict of interest.

References

1. Ma, X.; Yang, L.; Shang, X.; Li, M.; Gao, D.; Wu, C.; Zheng, S.; Zhang, B.; Chen, J.; Chen, C.; et al. Grain boundary defect passivation by in situ formed wide-bandgap lead sulfate for efficient and stable perovskite solar cells. *Chem. Eng. J.* **2021**, *426*, 130685. [[CrossRef](#)]
2. Chen, C.; Zheng, S.; Song, H. Photon management to reduce energy loss in perovskite solar cells. *Chem. Soc. Rev.* **2021**, *50*, 7250–7329. [[CrossRef](#)] [[PubMed](#)]
3. Jeon, N.J.; Noh, J.H.; Yang, W.S.; Kim, Y.C.; Ryu, S.; Seo, J.; Seok, S.I. Compositional engineering of perovskite materials for high-performance solar cells. *Nature* **2015**, *517*, 476–480. [[CrossRef](#)] [[PubMed](#)]
4. Liu, M.Z.; Johnston, M.B.; Snaith, H.J. Efficient planar heterojunction perovskite solar cells by vapour deposition. *Nature* **2013**, *501*, 395–398. [[CrossRef](#)]
5. Ummadisingu, A.; Steier, L.; Seo, J.-Y.; Matsui, T.; Abate, A.; Tress, W.; Grätzel, M. The effect of illumination on the formation of metal halide perovskite films. *Nature* **2017**, *545*, 208–212. [[CrossRef](#)]
6. Mei, A.; Li, X.; Liu, L.; Ku, Z.; Liu, T.; Rong, Y.; Xu, M.; Hu, M.; Chen, J.; Yang, Y.; et al. A hole-conductor-free, fully printable mesoscopic perovskite solar cell with high stability. *Science* **2014**, *345*, 295–298. [[CrossRef](#)]
7. Nie, W.; Tsai, H.; Asadpour, R.; Blancon, J.-C.; Neukirch, A.J.; Gupta, G.; Crochet, J.J.; Chhowalla, M.; Tretiak, S.; Alam, M.A.; et al. High-efficiency solution-processed perovskite solar cells with millimeter-scale grains. *Science* **2015**, *347*, 522–525. [[CrossRef](#)]
8. Samuel, D.; Stranks, G.E.E.; Grancini, G.; Menelaou, C.; Alcocer, M.J.P.; Leijtens, T.; Herz, L.M.; Petrozza, A.; Snaith, H.J. Electron-Hole Diffusion Lengths Exceeding 1 Micrometer in an Organometal Trihalide Perovskite Absorber. *Science* **2013**, *342*–343, 341–344. [[CrossRef](#)]
9. Yang, W.S.; Park, B.-W.; Jung, E.H.; Jeon, N.J.; Kim, Y.C.; Lee, D.U.; Shin, S.S.; Seo, J.; Kim, E.K.; Noh, J.H.; et al. Iodide management in formamidinium-lead-halide-based perovskite layers for efficient solar cells. *Science* **2017**, *356*, 1376–1379. [[CrossRef](#)]
10. Chen, C.; Li, H.; Jin, J.; Cheng, Y.; Liu, D.; Song, H.; Dai, Q. Highly enhanced long time stability of perovskite solar cells by involving a hydrophobic hole modification layer. *Nano Energy* **2017**, *32*, 165–173. [[CrossRef](#)]
11. Chen, C.; Li, H.; Jin, J.; Chen, X.; Cheng, Y.; Zheng, Y.; Liu, D.; Xu, L.; Song, H.; Dai, Q. Long-Lasting Nanophosphors Applied to UV-Resistant and Energy Storage Perovskite Solar Cells. *Adv. Energy Mater.* **2017**, *7*, 1700758. [[CrossRef](#)]
12. Chen, C.; Liu, D.; Zhang, B.; Bi, W.; Li, H.; Jin, J.; Chen, X.; Xu, L.; Song, H.; Dai, Q. Carrier Interfacial Engineering by Bismuth Modification for Efficient and Thermoresistant Perovskite Solar Cells. *Adv. Energy Mater.* **2018**, *8*, 201703659. [[CrossRef](#)]

13. Chen, J.; Zhao, X.; Kim, S.G.; Park, N.G. Multifunctional Chemical Linker Imidazoleacetic Acid Hydrochloride for 21% Efficient and Stable Planar Perovskite Solar Cells. *Adv. Mater.* **2019**, *31*, e1902902. [[CrossRef](#)] [[PubMed](#)]
14. Kim, G.-W.; Kang, G.; Kim, J.; Lee, G.-Y.; Kim, H.I.; Pyeon, L.; Lee, J.; Park, T. Dopant-free polymeric hole transport materials for highly efficient and stable perovskite solar cells. *Energy Environ. Sci.* **2016**, *9*, 2326–2333. [[CrossRef](#)]
15. Leijtens, T.; Eperon, G.E.; Pathak, S.; Abate, A.; Lee, M.M.; Snaith, H.J. Overcoming ultraviolet light instability of sensitized TiO₂ with meso-superstructured organometal tri-halide perovskite solar cells. *Nat. Commun.* **2013**, *4*, 2885. [[CrossRef](#)] [[PubMed](#)]
16. Li, M.; Zuo, C.; Hu, J.; Ding, L. Carrier management makes perovskite solar cells approaching Shockley–Queisser limit. *Sci. Bull.* **2021**, *66*, 1372–1374. [[CrossRef](#)] [[PubMed](#)]
17. Chen, C.; Liu, D.; Wu, Y.; Bi, W.; Sun, X.; Chen, X.; Liu, W.; Xu, L.; Song, H.; Dai, Q. Dual interfacial modifications by conjugated small-molecules and lanthanides doping for full functional perovskite solar cells. *Nano Energy* **2018**, *53*, 849–862. [[CrossRef](#)]
18. Chen, C.; Cheng, Y.; Dai, Q.; Song, H. Radio Frequency Magnetron Sputtering Deposition of TiO₂ Thin Films and Their Perovskite Solar Cell Applications. *Sci. Rep.* **2015**, *5*, 17684. [[CrossRef](#)]
19. Kim, H.; Lee, S.U.; Lee, D.Y.; Paik, M.J.; Na, H.; Lee, J.; Seok, S.I. Optimal Interfacial Engineering with Different Length of Alkylammonium Halide for Efficient and Stable Perovskite Solar Cells. *Adv. Energy Mater.* **2019**, *9*, 1902740. [[CrossRef](#)]
20. Yoo, J.J.; Wieghold, S.; Sponseller, M.C.; Chua, M.R.; Bertram, S.N.; Hartono, N.T.P.; Tresback, J.S.; Hansen, E.C.; Correa-Baena, J.-P.; Bulović, V.; et al. An interface stabilized perovskite solar cell with high stabilized efficiency and low voltage loss. *Energy Environ. Sci.* **2019**, *12*, 2192–2199. [[CrossRef](#)]
21. Liu, Z.; Qiu, L.; Ono, L.K.; He, S.; Hu, Z.; Jiang, M.; Tong, G.; Wu, Z.; Jiang, Y.; Son, D.-Y.; et al. A holistic approach to interface stabilization for efficient perovskite solar modules with over 2,000-hour operational stability. *Nat. Energy* **2020**, *5*, 596–604. [[CrossRef](#)]
22. Yusoff, A.R.b.M.; Nazeeruddin, M.K. Low-Dimensional Perovskites: From Synthesis to Stability in Perovskite Solar Cells. *Adv. Energy Mater.* **2018**, *8*, 1702073. [[CrossRef](#)]
23. Cheng, L.; Liu, Z.; Li, S.; Zhai, Y.; Wang, X.; Qiao, Z.; Xu, Q.; Meng, K.; Zhu, Z.; Chen, G. Highly Thermostable and Efficient Formamidinium-Based Low-Dimensional Perovskite Solar Cells. *Angew. Chem. Int. Ed. Engl.* **2021**, *60*, 856–864. [[CrossRef](#)] [[PubMed](#)]
24. Chen, K.; Wu, P.; Yang, W.; Su, R.; Luo, D.; Yang, X.; Tu, Y.; Zhu, R.; Gong, Q. Low-dimensional perovskite interlayer for highly efficient lead-free formamidinium tin iodide perovskite solar cells. *Nano Energy* **2018**, *49*, 411–418. [[CrossRef](#)]
25. Zhao, W.; Dong, Q.; Zhang, J.; Wang, S.; Chen, M.; Zhao, C.; Hu, M.; Jin, S.; Padture, N.P.; Shi, Y. Asymmetric alkyl diamine based Dion–Jacobson low-dimensional perovskite solar cells with efficiency exceeding 15%. *J. Mater. Chem. A* **2020**, *8*, 9919–9926. [[CrossRef](#)]
26. Lee, H.B.; Kumar, N.; Devaraj, V.; Tyagi, B.; He, S.; Sahani, R.; Ko, K.-J.; Oh, J.-W.; Kang, J.-W. Trifluoromethyl-Group Bearing, Hydrophobic Bulky Cations as Defect Passivators for Highly Efficient, Stable Perovskite Solar Cells. *Sol. RRL* **2021**, *5*, 2100712. [[CrossRef](#)]
27. Lee, H.B.; Kumar, N.; Tyagi, B.; He, S.; Sahani, R.; Kang, J.W. Bulky organic cations engineered lead-halide perovskites: A review on dimensionality and optoelectronic applications. *Mater. Today Energy* **2021**, *21*, 100759. [[CrossRef](#)]
28. Zai, H.; Su, J.; Zhu, C.; Chen, Y.; Ma, Y.; Zhang, P.; Ma, S.; Zhang, X.; Xie, H.; Fan, R.; et al. Sandwiched electrode buffer for efficient and stable perovskite solar cells with dual back surface fields. *Joule* **2021**, *5*, 2148–2163. [[CrossRef](#)]
29. Wei, N.; Chen, Y.; Miao, Y.; Zhang, T.; Wang, X.; Wei, H.; Zhao, Y. 5-Ammonium Valeric Acid Iodide to Stabilize MAPbI₃ via a Mixed-Cation Perovskite with Reduced Dimension. *J. Phys. Chem. Lett.* **2020**, *11*, 8170–8176. [[CrossRef](#)]
30. Wang, Y.; Zhang, T.; Kan, M.; Zhao, Y. Bifunctional Stabilization of All-Inorganic alpha-CsPbI₃ Perovskite for 17% Efficiency Photovoltaics. *J. Am. Chem. Soc.* **2018**, *140*, 12345–12348. [[CrossRef](#)]
31. Sutanto, A.A.; Drigo, N.; Queloz, V.I.E.; Garcia-Benito, I.; Kirmani, A.R.; Richter, L.J.; Schouwink, P.A.; Cho, K.T.; Paek, S.; Nazeeruddin, M.K.; et al. Dynamical evolution of the 2D/3D interface: A hidden driver behind perovskite solar cell instability. *J. Mater. Chem. A* **2020**, *8*, 2343–2348. [[CrossRef](#)]
32. Proppe, A.H.; Johnston, A.; Teale, S.; Mahata, A.; Quintero-Bermudez, R.; Jung, E.H.; Grater, L.; Cui, T.; Filleter, T.; Kim, C.Y.; et al. Multication perovskite 2D/3D interfaces form via progressive dimensional reduction. *Nat. Commun.* **2021**, *12*, 3472. [[CrossRef](#)] [[PubMed](#)]
33. Liu, Z.; Meng, K.; Wang, X.; Qiao, Z.; Xu, Q.; Li, S.; Cheng, L.; Li, Z.; Chen, G. In Situ Observation of Vapor-Assisted 2D-3D Heterostructure Formation for Stable and Efficient Perovskite Solar Cells. *Nano Lett.* **2020**, *20*, 1296–1304. [[CrossRef](#)] [[PubMed](#)]
34. Lin, Y.; Bai, Y.; Fang, Y.; Chen, Z.; Yang, S.; Zheng, X.; Tang, S.; Liu, Y.; Zhao, J.; Huang, J. Enhanced Thermal Stability in Perovskite Solar Cells by Assembling 2D/3D Stacking Structures. *J. Phys. Chem. Lett.* **2018**, *9*, 654–658. [[CrossRef](#)] [[PubMed](#)]
35. Ren, H.; Yu, S.; Chao, L.; Xia, Y.; Sun, Y.; Zuo, S.; Li, F.; Niu, T.; Yang, Y.; Ju, H.; et al. Efficient and stable Ruddlesden–Popper perovskite solar cell with tailored interlayer molecular interaction. *Nat. Photonics* **2020**, *14*, 154–163. [[CrossRef](#)]
36. Zheng, X.; Chen, B.; Dai, J.; Fang, Y.; Bai, Y.; Lin, Y.; Wei, H.; Zeng, X.C.; Huang, J. Defect passivation in hybrid perovskite solar cells using quaternary ammonium halide anions and cations. *Nat. Energy* **2017**, *2*, 17102. [[CrossRef](#)]
37. Ahmad, S.; Fu, P.; Yu, S.; Yang, Q.; Liu, X.; Wang, X.; Wang, X.; Guo, X.; Li, C. Dion–Jacobson Phase 2D Layered Perovskites for Solar Cells with Ultrahigh Stability. *Joule* **2019**, *3*, 794–806. [[CrossRef](#)]

38. Ke, W.; Mao, L.; Stoumpos, C.C.; Hoffman, J.; Spanopoulos, I.; Mohite, A.D.; Kanatzidis, M.G. Compositional and Solvent Engineering in Dion–Jacobson 2D Perovskites Boosts Solar Cell Efficiency and Stability. *Adv. Energy Mater.* **2019**, *9*, 1803384s. [[CrossRef](#)]
39. Gong, J.; Hao, M.; Zhang, Y.; Liu, M.; Zhou, Y. Layered 2D Halide Perovskites beyond the Ruddlesden–Popper Phase: Tailored Interlayer Chemistries for High-Performance Solar Cells. *Angew. Chem. Int. Ed. Engl.* **2022**, *61*, e202112022. [[CrossRef](#)]
40. Mao, L.; Ke, W.; Pedesseau, L.; Wu, Y.; Katan, C.; Even, J.; Wasielewski, M.R.; Stoumpos, C.C.; Kanatzidis, M.G. Hybrid Dion–Jacobson 2D Lead Iodide Perovskites. *J. Am. Chem. Soc.* **2018**, *140*, 3775–3783. [[CrossRef](#)]

Disclaimer/Publisher’s Note: The statements, opinions and data contained in all publications are solely those of the individual author(s) and contributor(s) and not of MDPI and/or the editor(s). MDPI and/or the editor(s) disclaim responsibility for any injury to people or property resulting from any ideas, methods, instructions or products referred to in the content.